The Planetary Science Journal, 6:269 (9pp), 2025 November https://doi.org/10.3847/PSJ/ae172f

High-temperature He^+ Irradiation of Low-iron-bearing Olivine: Laboratory Simulations of Space Weathering on Mercury

Surya Snata Rout[1,2], Ulrich Kentsch[3], Ralf Dohmen[4], Franziska Traeger[5], Swarna Prava Das[1], Hans-Werner Becker[6], Stefan Facsko[3], and Martin Ritter[7]
[1] School of Earth & Planetary Sciences, National Institute of Science Education and Research, Jatani, 752050 Khurda, Odisha, India; surya.rout@niser.ac.in
[2] Homi Bhabha National Institute, Training School Complex, Anushaktinagar, 400094 Mumbai, India
[3] Helmholtz-Zentrum Dresden-Rossendorf, Bautzner Landstraße 400, 01328 Dresden, Germany
[4] Institut für Geowissenschaften, Universitätsstr. 150, Ruhr-Universität Bochum, D-44801 Bochum, Germany
[5] Westfälische Hochschule, August-Schmidt-Ring 10, 45665 Recklinghausen, Germany
[6] RUBION Zentrale Einrichtung für Ionenstrahlen und Radionuklide, Universitätsstraße 150, Ruhr-Universität Bochum, D-44801 Bochum, Germany
[7] Electron Microscopy Unit, Hamburg University of Technology, Eißendorfer Straße 42, 21073 Hamburg, Germany
Received 2024 September 26; revised 2025 September 18; accepted 2025 October 18; published 2025 November 24

Abstract

The surface of Mercury is highly space weathered, and the products of space weathering are different than on the Moon. Here we simulate the interaction of solar wind ions with the surface of Mercury by implanting low-iron-bearing (∼3 wt% Fe) olivine slices with 4 keV He^+ ions both under ambient conditions and at 450 °C during the irradiation. The sample irradiated under ambient conditions shows a ∼140 nm thick partially amorphous layer on top of the grain with high concentrations of bubbles and cavities. However, the sample irradiated at 450 °C has a 110–140 nm thick polycrystalline layer with 1–5 nm sized nanoparticles of metallic iron and no bubbles or cavities. Mg atoms are preferentially sputtered from the ion-damaged layer present on the sample irradiated under ambient conditions, but no difference in composition is seen between the crystalline olivine and the ion-damaged layer in the sample irradiated at 450 °C. In addition, a thin amorphous film deposited on a micro-electromechanical systems–based chip is heated up to 1200 °C in situ inside a transmission electron microscope for a few milliseconds, and it produced nanoparticles of size 5–30 nm. Our results show that solar wind irradiation of low-iron-bearing olivine in the equatorial regions of Mercury will produce nanoparticles of iron whose sizes will be larger than that on the surface of the Moon and that the size will further increase during impacts of dust particles. Solar-wind-implanted He can diffuse out of regolith grains and can be a source of He observed in the exosphere of Mercury.

Unified Astronomy Thesaurus concepts: Mercury (planet) (1024); Solar wind (1534); Planetary surfaces (2113)

1. Introduction

Space weathering (SW) is an active process on the surface of many airless solar system bodies that are not protected by a magnetic field or an atmosphere to prevent the solar wind, cosmic rays, and micrometeorites from directly interacting with their surface (B. Hapke 2001; C. R. Chapman 2004; C. M. Pieters & S. K. Noble 2016). These interactions of solar and cosmic rays and micrometeorites cause physical and chemical alteration of the surface, impact vaporization, ion sputtering, and implantation, which leads to gardening and change in the optical properties of the surface materials. For the case of the Moon, the changes in optical properties of the surface or regolith include darkening and reddening (increase in the slope of the spectral continuum with increasing wavelength) of spectra, decrease in contrast of absorption bands in reflectance spectra, and brightening and straightening of spectral slope in the near-UV spectral range (C. M. Pieters et al. 1993; C. M. Pieters 1998; B. Hapke 2001). These effects have been well documented for the lunar soil samples, where the finer $<20\ \mu$m regolith grains show the strongest effects (C. M. Pieters et al. 1993, 2000; S. K. Noble et al. 2010). One of the accepted causes for the SW-induced optical alteration of the lunar regolith is the reduction of ferrous and ferric iron to nanophase metallic iron inclusions ($npFe^0$) within 60–200 nm thin amorphous films/patinas on the silicate and oxide mineral grains (L. P. Keller & D. S. McKay 1993, 1997). These films are produced during micrometeorite impact vapor and solar wind ion sputter deposition, and the size of $npFe^0$ within them ranges from 1 to 12 nm in diameter with a mean of 3 nm (L. P. Keller & D. S. McKay 1997; L. P. Keller & S. J. Clemett 2001; C. James et al. 2002, 2003). In addition, the reduction of ferrous and ferric iron takes place within the micrometeorite impact-generated melts (e.g., melt spherules and agglutinates within the lunar soil) owing to thermal reduction (L. P. Keller & D. S. McKay 1997; M. Yamada et al. 1999), and the size of iron inclusions within the lunar agglutinates ranges from 10 to 1500 nm (C. James et al. 2002, 2003). Although different processes have been proposed to explain the above SW-related features seen within lunar regolith (L. P. Keller & D. S. McKay 1997; B. Hapke 2001b), it is still debated which process dominates over the other. It is also contentious whether this model of lunar-like SW can be directly extrapolated to other solar system bodies. For example, recent analyses of the samples from the Itokawa asteroid have shown that the nature of the coatings on the Itokawa surface grains is different from what is seen on lunar samples, e.g., sizes of $npFe^0$ inclusions are smaller than in lunar soil grains, and the presence of nanophase sulfides (T. Noguchi et al. 2011, 2014; L. Chaves & M. Thompson 2022). Search for SW effects in lunar and other regolith breccia meteorites at least

qualitatively substantiates that a lunar-like SW process may be active on the surface of different asteroids, although the weathering products should be different (e.g., the presence of fewer impact melts and vapor deposits) owing to low impact velocity and less solar wind flux at asteroidal distances (S. K. Noble et al. 2005, 2010).

Although we now know much better how SW occurs on the Moon and near-Earth S-type asteroids, there is a lack of knowledge regarding the process of SW on other solar system bodies. The products of SW are directly related to various factors, such as surface composition, exposure time and resurfacing rates, location in the solar system (e.g., solar wind flux and micrometeorite flux and velocity), temperature, and strength of the magnetic field. For example, Mercury is most likely subjected to an intense SW owing to higher solar wind flux and faster micrometeoroid impacts (M. J. Cintala 1992). The UV to visible and near-IR (VNIR) spectrum of Mercury is red sloped and featureless, and the average albedo of Mercury is lower than that of the lunar nearside and similar to that of lunar maria except for the evidence for ferrous iron. Results from MESSENGER X-ray and gamma-ray spectrometers estimate the iron abundance on Mercury to be ~1–2 wt% (1.3–2.6 wt% FeO) and 1.4 ± 0.9 wt% of C (T. J. McCoy et al. 2018). The low iron concentrations on the surface of Mercury should consequently lead to low abundance of nanoparticles of iron as a result of SW. This makes it challenging to explain the cause of the low-albedo, red-sloped, and featureless spectra of Mercury in the VNIR region, if we assume that lunar-like SW is active on the surface of Mercury.

The study of lunar samples shows that reddening of the spectra in the VNIR region is primarily caused by $npFe^0$ particles <10 nm and darkening by particles >50 nm (S. K. Noble et al. 2007; P. G. Lucey & S. K. Noble 2008). In addition to that, the abundance of $npFe^0$ particles (<30 nm) is also a crucial factor that affects the reddening and darkening of the VNIR spectra. The abundance of $npFe^0$ particles is given by the maturity index I_s/FeO of a regolith, where I_s is the ferromagnetic resonance signal intensity (R. V. Morris 1978). One of the explanations for the strong reddening and darkening of the VNIR spectra of Mercury could be the presence of one or more opaque phases on Mercury that are absent on the Moon and the presence of large Britt–Pieters (B-P) Fe and opaque particles of >50 nm, along with nanophase iron ($npFe^0$) and nanophase opaque (npOpq) particles (<50 nm) hosted within agglutinates and as coating around regolith grains (P. G. Lucey & M. A. Riner 2011; L. V. Starukhina & Y. G. Shkuratov 2011; D. Trang et al. 2017). Additionally, Mercury's surface temperatures can reach up to approximately 450 °C at the equatorial regions and the hot poles during the day (K. E. Bauch et al. 2021) but can drop to around −180°C during the night. Due to the high temperatures, any nanophase iron inclusions that may be present within the nanometer-thick films and melt layers around regolith grains can grow in size owing to the process of Ostwald ripening (S. K. Noble & C. M. Pieters 2003), but this has not yet been experimentally proven. There has also been an observed correlation between latitudinal and longitudinal surface temperature variation on Mercury and the mean surface reflectance and spectral slope (D. Trang et al. 2017; J. T. Wilson et al. 2019; A. N. Deutsch et al. 2024). The cause for this correlation is again attributed to the increase in size of the nanoparticles of iron due to Ostwald ripening, although it has to be experimentally proved that nanoparticles of iron can grow to larger sizes through the diffusion-related Ostwald ripening process. Another way of producing larger nanoparticles of iron is through growth during repeated melting due to micrometeorite impacts. But there is no observed variation in flux of micrometeorites with latitude and longitude on the surface of Mercury, and therefore micrometeorite impact cannot be used for explaining the variation in size of nanoparticles with latitude or longitude. However, all these observations are proof that temperature is a crucial factor affecting the products of SW on Mercury.

Different laboratory experiments have successfully simulated the process of micrometeorite impact heating and solar wind interactions using a nanosecond pulsed laser and energetic ions, respectively (G. Wehner et al. 1963; D. Rosenberg & G. Wehner 1964; B. Hapke 1965, 1966, 1968, 1973, 2001; C. E. KenKnight et al. 1967; D. B. Nash 1967; L. Yin et al. 1972, 1975; B. Hapke et al. 1975; C. A. Dukes et al. 1999; M. Yamada et al. 1999; S. Sasaki et al. 2002; R. Brunetto & G. Strazzulla 2005; M. J. Loeffler et al. 2009; C. Lantz et al. 2017; M. S. Thompson et al. 2019; D. L. Laczniak et al. 2021). These simulations have helped in understanding the rates and effects of SW and the changes in different mineral phases during SW. However, there are few studies that directly simulate the process of SW on the surface of Mercury (L. V. Moroz et al. 2014; M. S. Thompson et al. 2021; A. N. Stojic et al. 2023; I. Weber et al. 2023; N. Bott et al. 2024; E. Caminiti et al. 2024), and laser and ion irradiation of Mercury-analog materials are needed. Additionally, the high temperature on the surface of Mercury can lead to changes in amorphous rims formed around the regolith grain and melts produced owing to the impact of micrometeorites: crystallization of amorphous rims, and growth of $npFe^0$, B-P particles, or FeS. There is also a lack of clear understanding of the chemical and mineralogical changes during ion-induced sputtering of silicate and oxide minerals at ambient and high-temperature conditions. This knowledge is crucial to understand the formation process of nanoparticles of different species and also the nature of amorphous layers on regolith grains of different solar system bodies.

In this study, we simulate the interaction of solar wind ions with low-iron-bearing olivine at 450 °C that is relevant for the dayside equatorial region and hot poles of Mercury. The motivations of this study are understanding (a) the effect of temperature, relevant to the surface of Mercury, on the product of ion irradiation of silicate minerals with low iron content; (b) chemical and structural changes within the ion-damaged surface layers of low-iron-bearing silicate minerals; and (c) the growth process of iron nanoparticles at high temperatures.

2. Experimental Procedures and Analytical Techniques

2.1. Sample

A pale-green-colored olivine crystal from a locality in Pakistan obtained from the Mineralogical Museum of the University of Würzburg, Germany, was used for the experiment. The sample was cut into two 2 mm thick slices and polished. After polishing, the sample was ultrasonically cleaned using deionized water and isopropanol to remove any contamination and organics on the surface. Details about the samples used in this study are provided in Table 1. The elemental composition of the samples was previously characterized using an electron microprobe, and the measured composition is given in Table 2.

Table 1
List of Samples Used for This Study

Samples	Description
Olivine crystal (U-olivine)	Olivine crystal irradiated with 4 keV He^+ ions under ambient conditions
Olivine crystal (H-olivine)	Olivine crystal irradiated with 4 keV He^+ ions under 450 °C
MEMS chips	Four MEMS chips deposited with 80 nm thick amorphous film from a San Carlos olivine sample using the PLD technique
MEMS chips	Four MEMS chips with amorphous film annealed at 500 °C, 550 °C, 600 °C, and 700 °C for 48, 72, 72, and 48 hr, respectively

Table 2
Representative Composition of the Lamella Prepared from a U- and H-Olivine Sample Measured Using TEM-EDS

		U-olivine		H-olivine (Sample at 450 °C)	
	Olivine[a]	Olivine (Crystalline)[b]	Olivine (Amorphous)[c]	Olivine (Crystalline)[b]	Olivine (Amorphous)[c]
Si	19.8	19.1	20.9	20.6	21.6
Mg	32.6	33.2	31.2	31.5	30.3
Fe	3.1	3.2	2.7	2.9	2.7
Ni	0.33	n.a.	n.a.	n.a.	n.a.
O	44.2	44.5	45.2	45.0	45.4
Total	100.00	100.0	100.0	100.0	100.0
		Number of Cations per Formula Unit (Normalized to Four Oxygen)			
Si	1.00	0.97	1.08	1.06	1.12
Mg	1.91	1.95	1.86	1.87	1.81
Fe	0.08	0.08	0.07	0.08	0.07
Ni	0.004	n.a.	n.a.	n.a.	n.a.
Total	2.994	3.00	3.01	3.01	3.00
O/Si	2.2	2.3	2.2	2.2	2.1
Mg/Si	1.7	1.7	1.5	1.5	1.4

Note. Concentration is in wt%, and associated errors (for measurement done with TEM-EDS) are ∼10%.
[a] Composition of the unirradiated olivine measured using an electron microprobe. n.a. = not analyzed.
[b] Composition of the crystalline region of the lamella/olivine (e.g., Figures 1(a), (b)).
[c] Bulk composition of the amorphous ion-damaged layer above the crystalline region (e.g., Figures 1(a), (b)).

2.2. Ion Implantation

Ion implantation was done at the Ion Beam Center (IBC), Helmholtz-Zentrum Dresden-Rossendorf, with He^+ at 4 keV using a fluence of 5×10^{17} ions cm^{-2}. The current density during the experiment was kept at $<1\ \mu A\ cm^{-2}$ to prevent overheating of the sample. Keeping all the parameters the same, one crystal was irradiated under ambient temperature (U-olivine), the second sample was kept at 450 °C (H-olivine), and temperature was controlled during the whole duration of the ion irradiation.

2.3. Focused Ion Beam Scanning Electron Microscopy and Transmission Electron Microscopy

Samples for transmission electron microscopy (TEM) were prepared from the two irradiated olivine crystals using a conventional in situ lift-out technique using a Helios Nanolab G3 UC focused ion beam scanning electron microscope from Thermo Fisher Scientific. A total of two lamellae (one each from the sample irradiated at ambient conditions and from the sample irradiated at 450 °C) were prepared and studied at the Electron Microscopy Unit (BEEM), Hamburg University of Technology, using a Talos F200X TEM operating at 200 kV. The TEM is equipped with a high-brightness Schottky-FEG (X-FEG), scanning TEM–high-angle annular dark field (STEM-HAADF) detector, and four-quadrant silicon drift detector - energy-dispersive X-ray spectroscopy system (solid angle of 0.9 sr), which was used for energy-dispersive X-ray spectroscopy (EDS) analysis. Spectral images were obtained with a probe current of ∼150 pA and a dwell time of 10–20 μs per pixel. Different standards were used for measuring the *k*-factors (N. J. Zaluzec 1979) of Mg, Si, and Fe: UWCr-3 chromite (P. R. Heck et al. 2010), North Chile IIAB iron meteorite (Field Museum ME2595), and a polished piece of the unirradiated olivine slice used in the present irradiation experiment. The software Velox (Thermo Fisher Scientific) was used for data acquisition, EDS quantification, and visualization.

2.4. Pulsed Laser Deposition

The pulsed laser deposition (PLD) setup at the Ruhr-University of Bochum was used to deposit thin films directly on micro-electromechanical systems (MEMS) microheaters/chips (Table 1). A 193 nm (ArF) excimer laser was used to irradiate a San Carlos olivine (∼9 wt% FeO) at a frequency of 10 Hz (pulse duration 30 ns) and a laser fluence of $3\ J\ cm^{-2}$ under a vacuum of 10^{-5} Pa. The actual energy flux at the target surface can be controlled by an aperture or focusing lens. The MEMS microheaters/chips are placed on a ceramic quartz glass at about 45 mm distance from the target. The geometry is arranged such that the laser hits the target at about a 25° angle (with respect to the horizontal plane), and the substrates are placed directly in the path of the plasma coming out of the target at right angles to the surface (for details of the PLD setup, see R. Dohmen et al. 2002). The target itself is rotated

about an axis such that the laser is scanned over the surface of the target during ablation. The crucible containing the substrates sits on a SiC heater, which is capable of heating the substrates to temperatures up to 1000°C within a few minutes. The substrate was heated up to 450 °C during the deposition of the films, to simulate the effect of micrometeorite impact ejecta deposition on the hot surface of Mercury. We used San Carlos olivine as opposed to the low-iron-bearing olivine used in the irradiation study because the former has higher iron concentrations (9–10 wt% FeO). The high iron concentration should consequently produce a film with higher FeO, and the density of nucleating nanoparticles of iron should also be higher. The growth process of iron particles, if controlled through the diffusion process, can then be experimentally simulated in a reasonable amount of time.

2.5. In Situ TEM Annealing

Using the PLD technique, thin (80 nm) films were deposited on top of MEMS microheaters. The MEMS microheaters/chips are 8 mm × 3.3 mm in dimension and made of silicon. Within the silicon substrate, there is a window with a SiN membrane where the heating element is embedded. The heating element consists of four contact pads that are connected to a circular heating element that is heated through the joule effect when current is passed through the circular heating element. Within the circular/spiral heating element, there is a 100 um circular plate with 22 holes of 5 um diameter each that consists of an amorphous SiN membrane of 15 nm thickness and is transparent to electrons. There is a 15 nm thin holey SiN membrane within these 22 holes, and only the thin film deposited within this window was electron transparent. The MEMS chips were attached to a NanoEX-i/V single-tilt holder from Thermo Scientific, and the heating experiments were done in the Talos TEM with an external Keithley temperature controller. The amorphous films were then flash-heated at 1200°C (maximum temperature reached by the heater) for 0.5 s. After that, the films were annealed at various temperatures: 96 hr at 500°C, 72 hr at 550°C, 72 hr at 650°C, and 48 hr at 700°C. Temperatures were ramped with 1°C s^{-1} in steps of 50°C. Once a particular temperature is reached, 5 minutes are given for the temperature to stabilize. Only that part of the film was studied that was deposited on the 5 μm diameter holes with a 15 nm thick SiN membrane.

3. Results

3.1. He^+ Irradiation of Olivine under Ambient Conditions

Bright-field TEM (BF-TEM) images of lamella prepared from unheated (U)-olivine irradiated with He^+ ions show a ∼130–140 nm thick amorphous layer with numerous vesicles on top of the crystalline olivine (Figure 1(a)). The amorphous layer can be divided into two sublayers: sublayer 1 and sublayer 2. Sublayer 1 is 30–35 nm thick, has vesicles of 1–10 nm diameter, and is present directly above the crystalline olivine substrate. Sublayer 2 is ∼120 nm thick, overlies sublayer 1, and has high concentrations of vesicles whose size ranges up to 120 nm. Numerous linear and planar dislocations are observed in the crystalline olivine substrate. High-resolution TEM (HRTEM) imaging shows that the olivine substrate is crystalline (Figure 1(c)), but the overlying ion-implanted layer is partially amorphous with some nanocrystallites of olivine (Figure 1(c)). Bulk composition of the partially amorphous region taken using TEM-EDS has similar composition to the crystalline substrate (Table 2). However, the TEM-EDS line profile taken from the crystalline olivine substrate to the top of the amorphous layer shows some variations in distribution of elements (Figures 2(a), (b)) within the amorphous layer. The concentration of O does not show variations in the amorphous layer, but silicon shows an increase in concentration from 19 wt% in the crystalline part to 23 wt% at the interface with the amorphous ion-damaged layers; it then drops back to ∼19 wt% and finally again increases to 23 wt% at the top of the irradiated layer (Figure 2(b)). Magnesium, on the other hand, shows an opposite behavior to Si: concentration changes from ∼34 wt% in the crystalline substrate to ∼28 wt% at the interface, then gradually increases to ∼35 wt%, and finally decreases to 30 wt% (Figure 2(b)). For the elemental ratios, Mg/Si changes from 1.8 in the crystalline part to 1.2 at the interface with the overlying amorphous regions, increases to 1.9, and then decreases back to 1.4 (Figure 2(c)). The O/Si ratio exhibits similar variation to Mg/Si. The ratio of O/Mg shows variation from 1.3 in the crystalline part to 1.5 at the interface, then going to 1.2 and finally to 1.4 in the upper part of the amorphous layer (Figure 2(c)). For all of the above element concentrations and ratios the mean values at each pixel in the line profile are taken. However, no clear variation in concentration of elements is observed if an analytical error of ∼10% is taken into account.

3.2. He^+ Irradiation at 450 °C

The lamella prepared from olivine heated to 450 °C and irradiated with He^+ (H-olivine) shows the presence of a polycrystalline layer that is 110–140 nm (Figures 1(b), (d)) on top of the crystalline olivine and has a discontinuous interface between the crystalline olivine and the overlying polycrystalline region (Figure 1(d)). The discontinuous interface and the difference in thickness of the ion-damaged region are clearly illustrated in Figure 1(b). Numerous nanoparticles of Fe, identified using TEM-EDS, are concentrated in the top 50–60 nm of the polycrystalline layer (Figures 2(d), (f)). The size of Fe nanoparticles ranges between 1 and 5 nm. The diffraction pattern taken from the ion-damaged layer shows broadened diffraction maxima and the presence of various olivine crystallite islands that are preferentially arranged to exhibit a single crystal diffraction pattern the same as the underlying olivine crystal (Figure 1(d)). TEM-EDS line profiles acquired from the crystalline substrate to the polycrystalline ion-damaged layer show that the compositions of both regions are similar (Figure 2(e)). Only the top 10 nm region in the polycrystalline layer has depletion of the Si and Fe and enrichment of Mg, if their mean concentration values at each point/pixel are taken. But due to the high errors (10%) associated with the measurements, we cannot definitively say that there are actual variations in concentration of these elements.

3.3. Annealing of Amorphous Film Prepared Using PLD

The oxide thin film deposited on the MEMS-chip at 450 °C shows the presence of numerous nanoparticles of metallic Fe that are <1 nm in size (Figure 3). A high-resolution image of the sample could not be acquired, due to its rapid damage under the electron beam. For the same reason, the composition of the film could not be reliably measured. After flash annealing all four thin films at 1200°C for a few milliseconds, they transformed into an amorphous film with many

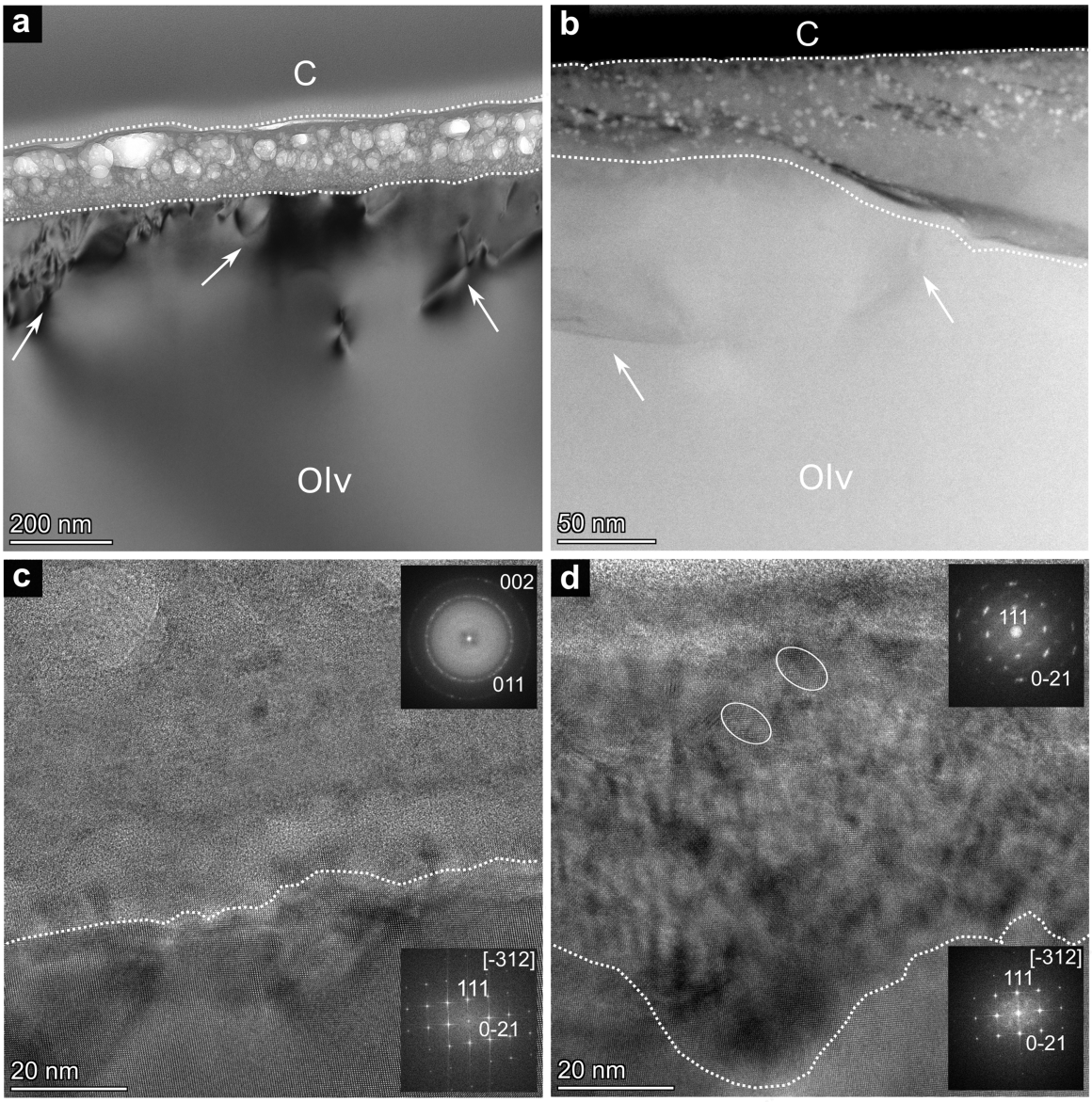

Figure 1. (a) BF-TEM image of the lamella prepared from U-olivine crystal. The layer with numerous vesicles on top of the crystalline olivine (Olv) is marked with dashed lines. Various dislocations in the olivine crystal are indicated with arrows. C = combination of sputter deposited carbon and carbon deposited from a precursor gas using a gas-injection system (GIS) attached to the focused ion beam instrument. (b) STEM-HAADF image of the lamella from H-olivine (irradiated at 450 °C). The ion-damaged region is marked with dashed lines and is characterized by the presence of numerous bright nanoparticles. (c) HRTEM image of a region from panel (a), showing the interface (dashed line) between crystalline olivine and the overlying ion-damaged region. Crystal lattice fringes are seen in the crystalline olivine, and the inset is the fast Fourier transform (FFT) of the crystalline and the overlying partially amorphous region. (d) HRTEM image of a region from panel (b) illustrating the polycrystalline ion-damaged layer and the underlying crystalline olivine. The interface between crystalline olivine and the ion-damaged layer is marked with a dashed line. The inset shows the FFT of the crystalline olivine and the ion-damaged region. The circled regions within the polycrystalline layer point to islands of olivine crystallites.

nanoparticles of Fe of size between 5 and 30 nm (Figure 3(b)). All four of these MEMS chips with 5–30 nm sized nanoparticles showed no further change in the size of the nanoparticles after annealing at 500 °C, 550 °C, 600 °C, and 700 °C for 48, 72, 72, and 48 hr, respectively. No changes were seen either in the amorphous matrix of the flash-annealed thin films after annealing, except for some small regions that crystallized after annealing for 48 hr at 700 °C.

4. Discussions

This study focuses on understanding the nature and abundance of nanoparticles around solar-wind-irradiated silicate mineral grains on the surface of Mercury. The high dayside temperatures and the variation of surface temperature with latitude and longitude on Mercury can play an important role in the nature and formation of nanoparticles during solar wind irradiation and micrometeorite impact, and this study investigates the former process, along with the effects of rapid heating events (e.g., micrometeorite impacts) on the products of ion irradiation. We first discuss the changes in surface properties of olivine grains, with low iron contents, due to ion irradiation under ambient and high temperatures and then the effects of micrometeorite-impact-related flash heating on the ion-damaged surface regions. The findings are compared with previous experimental ion irradiation studies, and we finally discuss their implications for understanding SW on Mercury.

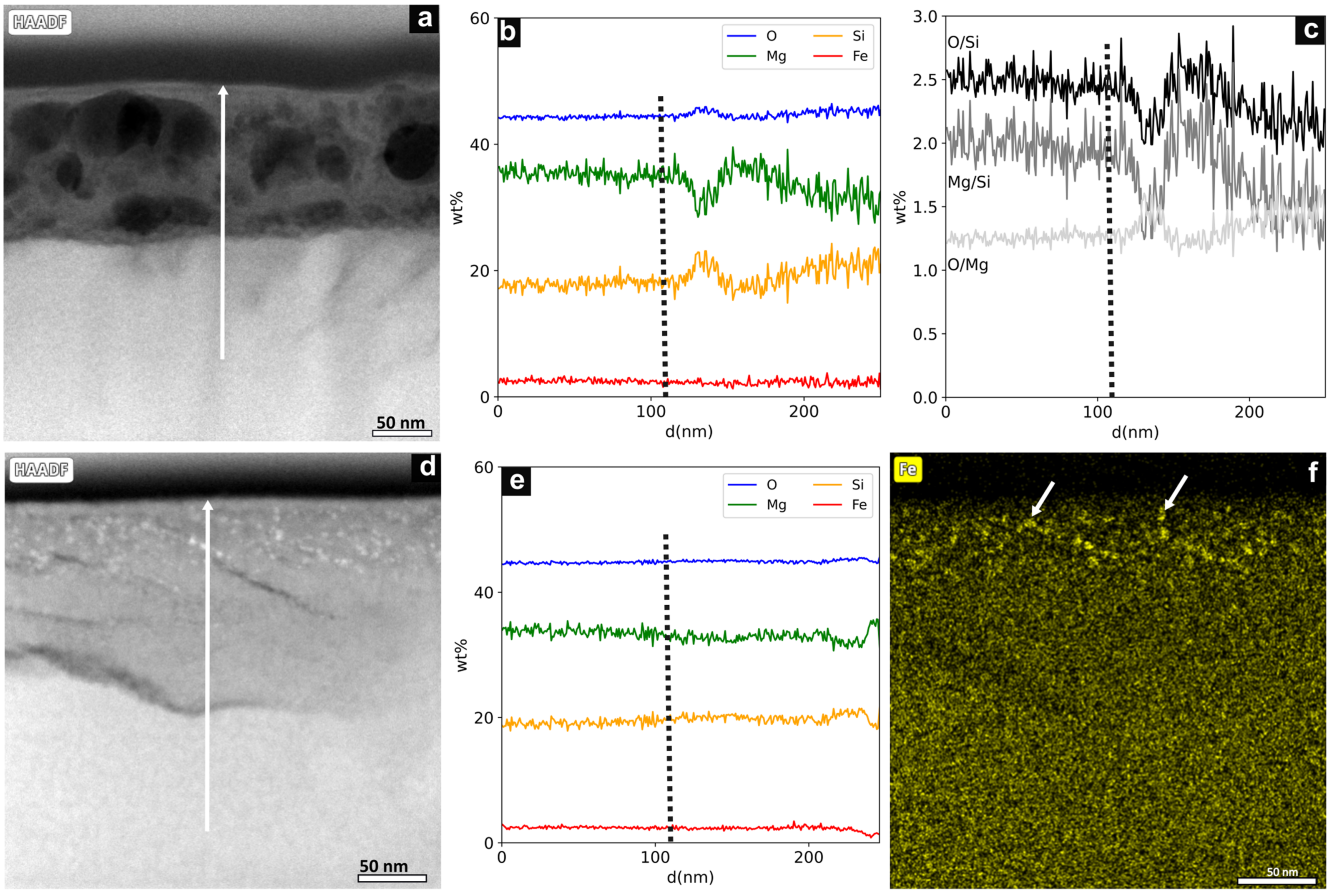

Figure 2. (a) STEM-HAADF image of a region of the lamella prepared from U-olivine. Line profiles extracted from TEM-EDS spectrum image (SI) obtained from the region in panel (a) show the variation in (b) element distribution and (c) element ratios from the interior of the irradiated grain to the surface as marked by the arrow in panel (a). (d) STEM-HAADF image of a region of the lamella prepared from H-olivine. (e) The line profile extracted from TEM-EDS SI of the region in panel (d) shows the variation in element distribution from the interior of the irradiated grain to the surface as marked by the arrow in panel (d). The dashed line in panels (b) and (e) marks the position of the interface between the crystalline part of the grain and the ion-damaged region. (f) TEM-EDS SI for element Fe (FeKα) from the region in panel (d) showing the distribution of Fe-rich nanoparticles (marked with arrows) on the top surface of the lamella.

4.1. Effects of Ion Irradiation on the Surface of Silicate Grains

Chemical changes in ion-damaged regions of a sample are primarily due to elastic sputtering of elements, leading to formation of defects and vacancies. During the sputtering process, there is selective ejection of atoms, recoil mixing, and diffusion. Selective/preferential sputtering is dependent on the energy of impacting ions and in the bonding state of the elements and is predominant in the energy range of 1–10 keV. For a certain material lighter atoms are preferentially sputtered and also reimplanted into deeper regions owing to impact with the incoming ions (P. Sigmund 1979). Finally, after a long duration of irradiation/high ion fluence, the whole ion-damaged layer shows chemical zonation, due to the interplay of preferential sputtering, reimplantation, and recoil mixing of elements. More dedicated experiments are needed to understand the effect of preferential sputtering and reimplantation within ion-damaged layers in silicate minerals. In the present study the element composition acquired from the ion-damaged region of the olivine slices has high uncertainties, but we can still use it for qualitative understanding of the effect of interaction of He ions with olivine under ambient and high-temperature conditions. In the olivine sample irradiated under ambient conditions (U-olivine), there is a clear decrease in concentration of Mg and an increase in concentration of Si at the interface between the crystalline undamaged olivine substrate and the ion-damaged amorphous layer (Figure 2(b)). Such a depletion of Mg and enrichment of Si were also seen within studied samples from asteroid Itokawa, in interplanetary dust particles, and in artificially irradiated olivine (J. P. Bradley 1994; J. Bradley & T. Ireland 1996; P. Carrez et al. 2002; J. Bradley & H. Ishii 2008; T. Noguchi et al. 2011, 2014; C. Jäger et al. 2016; M. S. Thompson et al. 2014, 2022). This zonation of elements is attributed, by previous studies, to a combined effect of preferential sputtering, sputter redeposition, recoil mixing, and enhanced diffusion of elements due to formation of radiation-induced defects. However, temperatures of the surfaces of asteroids are $<$200 °C, and at such low temperatures diffusion of elements is too slow. The absence of such distinct zonation of elements within the ion-damaged layer in the H-olivine of our study (Figure 2(e)) shows that diffusion is indeed an important process at high temperatures. However, the presence of dislocations and defects can aid the diffusion of ions at low temperatures, and this needs to be further studied using careful experiments and irradiation at different temperature steps.

The total implantation depth of 4 keV He^+ ions in olivine from the Stopping and Range of Ions in Matter (SRIM) computer code (see J. F. Ziegler & J. P. Biersack code http://www.srim.org/) calculations is ~140 nm, and the maximum ion implantation occurs at ~70 nm. According to this, we

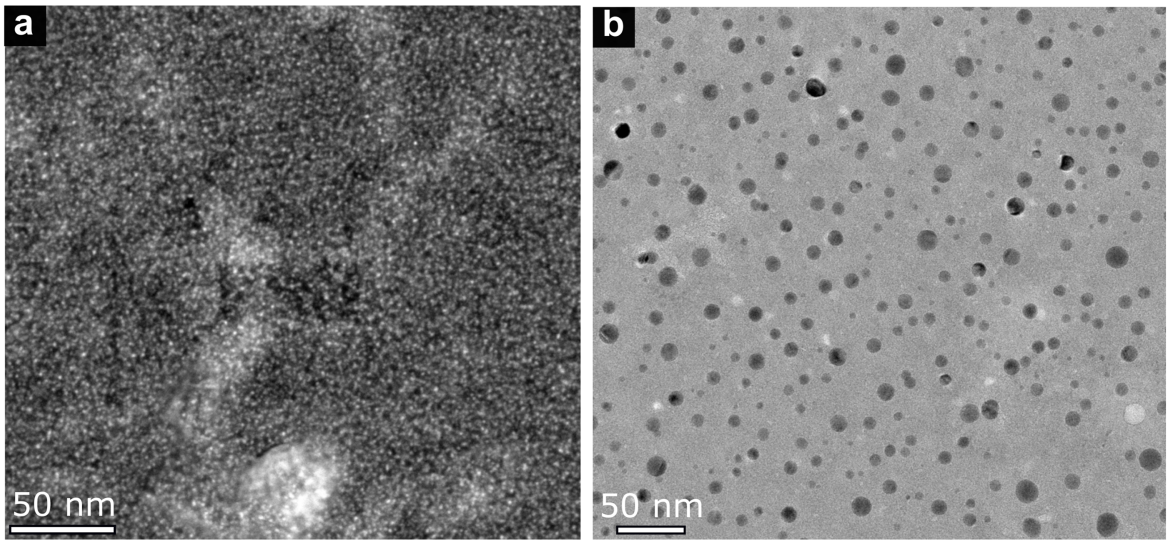

Figure 3. (a) STEM-HAADF image of the film deposited using the PLD technique on a MEMS-based chip for an in situ TEM annealing experiment. The film was deposited at 450 °C, and the bright regions are <1 nm sized Fe-rich inclusions present in a dark amorphous matrix. (b) BF-TEM image of the film shown in panel (a) after being heated for a few milliseconds up to 1200 °C. The spherical inclusions with dark contrast are Fe-metal particles.

should see the highest depletion of preferentially sputtered Mg atoms at ∼70 nm, but our data reveal that it is at 130–140 nm. This shows that the sputtered Mg atoms from 70 nm were reimplanted in the layer above it, leading to recoil mixing and homogenization. The highest depletion of Mg at 130–140 nm was established owing to sputtering by the deepest implanted He ions, and there was no recoil implantation of Mg atoms from deeper layers that could help in equilibration of the Mg concentration. Since Mg–O has weaker bond strength than Si–O, we see the highest depletion of Mg in the amorphous layer and a corresponding enrichment of Si (Figure 2(b)). Another observation that supports the preferential sputtering of Mg is the enrichment of Mg and depletion of Si in the top 10 nm of the ion-damaged layer (Figure 2(e)). This is most likely a product of redeposition of sputtered material where the concentration of Mg should be higher than that of Si. Similar observations were also seen in previous studies of naturally and artificially irradiated minerals (T. Noguchi et al. 2014; M. S. Thompson et al. 2014; D. L. Laczniak et al. 2021). However, surfaces of ion-irradiated samples are highly reactive and can oxidize rapidly or be affected by various other surface chemical effects related to different adsorbed atmospheric species (e.g., OH).

4.2. Effect of Temperature on Space-weathered Rims

From our experimental observations it is apparent that nanoparticles of iron can readily form in the 100–200 nm ion-damaged surface layer of olivine crystal slices after being irradiated at 450 °C (H-olivine; Figure 1(b)) with He^+ ions but not in olivine irradiated under ambient conditions (Figure 1(a)). These nanoparticles can further increase in size owing to any additional rapid heating events (e.g., micrometeorite impacts; Figure 3). Additionally, no bubbles are seen within the ion-damaged layer of H-olivine. The thickness of the ion-damaged layer is variable in the H-olivine, and similar variability is seen in artificially and naturally irradiated materials (T. Noguchi et al. 2014; M. S. Thompson et al. 2014; D. L. Laczniak et al. 2021). However, the causes of variation in thickness of ion-damaged layers are not very clear.

Observations from study of H-olivine show that temperature is one of the critical factors in (a) formation of nanoparticles, (b) diffusion-related homogenization of elements within ion-damaged regions of space-weathered samples, and (c) formation of bubbles.

The size of the observed nanoparticles is larger compared to that in the space-weathered rims of lunar soil grains, which show a mean size of ∼3 nm (L. P. Keller & S. J. Clemett 2001). The formation of nanoparticles of Fe in the H-olivine sample and the similarity in composition of the ion-damaged layer and the undamaged H-olivine substrate are directly related to the defects (e.g., vacancies, divacancies, and interstitials) produced owing to the impacting He^+ ions and the enhanced diffusion of Fe and He at high temperatures. During ion irradiation at room temperature, numerous defects and vacancies are produced, but the concentration is less when the temperature of the substrate is high during irradiation (V. Raineri et al. 2000). This shows that at high temperatures the defects either are annealed or combine with other interstitial defects (P. F. P. Fichtner et al. 2000; V. Raineri et al. 2000; M. David et al. 2003). Therefore, during irradiation of the H-olivine sample, vacancies caused by sputtered Mg, Si, and O atoms are subsequently replaced by diffusing Fe atoms, and gradual growth of the nanoparticles happens, as also seen in Fe-Si alloys (e.g., Y. Shimada et al. 2022). Since nanoparticles of Fe are observed in the sample, this shows that Fe is less preferentially sputtered and diffuses faster compared to Si and Mg at 450 °C. Finally, the enhanced diffusion of elements at 450 °C also leads to homogenization of the concentration of elements within the ion-damaged region.

During irradiation at high temperatures, He outgassing from the sample and migration of vacancies and defects to the surface of the sample can also happen (G. Cerofolini et al. 2000; K. Ono et al. 2019). Helium has very low solubility in crystalline silicon, and due to its inert nature, it does not interact with neighboring atoms. In addition, at high temperature the permeability of He in silicon is increased. The threshold fluence for formation of bubbles in silicon has been found to be 1×10^{16} ions cm^{-2} (P. F. P. Fichtner et al. 2000; V. Raineri et al. 2000; G. Cerofolino et al. 2000; M. David et al. 2003; K. Ono et al. 2019). The formation and growth of

bubbles are related to the formation of defects (vacancies and divacancies) during ion irradiation and its interaction with interstitial He. Helium primarily stays in the interstitial positions in the lattice and bonds with single vacancies or divacancies to gradually grow to He clusters and to finally form bubbles above the threshold dose. Density of bubbles is related to the concentration of vacancies, and therefore with an increase in depth of implantation the concentrations of vacancies and bubbles both decrease. But irradiation at high temperatures (>200 °C) leads to gradual annealing of defects, to decreases in density of He-filled bubbles, and also to diffusive loss. Silicon irradiated with a fluence of 5×10^{16} ions cm^{-2} and 9×10^{16} ions cm^{-2} shows an absence of He-filled bubbles at >800 °C and >400 °C, respectively (K. Ono et al. 2019). However, in our study we see an absence of He-filled bubbles at 450 °C, but the irradiation fluence is higher (e.g., 5×10^{17} ions cm^{-2}). More future experiments at different temperatures need to be done to understand the formation and diffusion process of He in ion-damaged amorphous regions. Finally, our observations show that He effectively diffused out of the H-olivine sample during ion irradiation, due to its increased permeability compared to ambient conditions.

4.3. Space Weathering on Mercury

Various evidences show that the surface of Mercury is highly space weathered. The featureless and red-sloped spectra of the surface of Mercury in the VNIR range point to a high degree of SW, which is different than what is observed on the Moon and asteroids, especially due to the low iron content within the regolith grains of Mercury. The optical effects of SW in the VNIR region are significantly affected by the size and abundance of nanoparticles around and within regolith grains and agglutinates, and this should also be the case for Mercury. The surface temperature on Mercury is also a critical factor that enhances the effects of SW. Evidence for this has been found through variation in spectral slope and albedo with latitude and longitude. Although this is attributed to a possible increase in size of nanoparticles of iron due to Ostwald ripening, there have been no experimental results to support it. The observations from our experiment show that ion irradiation at 450 °C can produce up to 5 nm sized nanoparticles of iron on the surface of regolith grains on Mercury and can be a factor that is responsible for the observed variation in spectral properties with latitude and longitude on the surface of Mercury. Although the weak magnetic field of Mercury shields the surface from solar wind ions, the magnetosphere is open to solar wind ions around the cusps, which leads to direct interaction of solar wind ions with the surface of Mercury at latitudes between 40° and 60° (E. Kallio & P. Janhunen 2003; P. Wurz et al. 2019). The temperatures at these latitudes can go up to 400 °C (K. E. Bauch et al. 2021). Additionally, the fast solar wind and, during coronal mass ejection events, the solar wind ions can directly interact with the whole surface of Mercury.

In addition to the solar wind ion implantation, the other products of SW on Mercury are melt particles due to the impact of dust particles. Spectral modeling shows that high concentrations of npFe^0 and npOpq (C) of 1–100 nm size and B-P particles (Fe and C) of >100 nm size are needed to successfully model the VNIR spectra of Mercury (P. G. Lucey & M. A. Riner 2011; L. V. Starukhina & Y. G. Shkuratov 2011; D. Trang et al. 2017). The primary hosts for these nano- and microparticles are most likely the melt produced owing to impact of dust particles on the surface of Mercury. In addition to that, our study shows that solar wind irradiation of Fe-poor silicate minerals will also be an important source for large nanoparticles (i.e., npFe^0 and npOpq). These nanoparticles can increase to the range of B-P particles during repeated impact of dust particles on the solar-wind-irradiated grains or during heating of adjacent grains present at the point of impact of dust particles. This is demonstrated by our results from flash heating of thin amorphous films, after which 1–2 nm sized nanoparticles of Fe grew to larger sizes (Figure 3). In addition to the impacting dust particles, the high temperature on Mercury could lead to Ostwald ripening and coarsening of npFe^0 and npOpq particles. However, experimental data on the behavior of npFe^0 and npOpq within a Si-rich glassy matrix are lacking. S. K. Noble & C. M. Pieters (2003) theoretically showed that Ostwald ripening can lead to an increase in the size of the npFe^0 inclusions, but their calculations had large uncertainties owing to poorly constrained parameters. The size of nanophase iron inclusions significantly affects the visible and near-infrared spectra (S. K. Noble et al. 2007; L. V. Starukhina & Y. G. Shkuratov 2011), with the small (<20 nm) npFe^0 inclusions causing darkening, reddening, and suppression of the absorption bands in the UV–visible spectral range. Future experiments need to be done to experimentally measure the diffusion coefficient and surface energy of npFe^0 and npOpq, both of which are temperature dependent. Finally, a combined effect of solar wind irradiation at elevated temperatures, micrometeorite impact melting and heating, and possible Ostwald ripening can lead to a change in size and an abundance of nanoparticles on the surface of Mercury, and this in turns leads to the observed variation in optical properties of the surface of Mercury with latitude and longitude.

Very few laser and ion irradiation experiments to simulate SW on Mercury-analog materials have been carried out until now (e.g., L. V. Moroz et al. 2014; M. S. Thompson et al. 2021; A. N. Stojic et al. 2023; I. Weber et al. 2023; N. Bott et al. 2024; E. Caminiti et al. 2024). In addition, none of the ion and laser experiments were carried out at temperatures matching the highest temperature reached on the surface of Mercury. Previous laser irradiation of Fe-poor plagioclase and quartz (L. V. Moroz et al. 2014; M. J. Loeffler et al. 2016) shows minor reddening of the spectra, primarily due to the very low abundance of npFe^0. The products of laser irradiation may not be strongly dependent on the temperature of the sample/substrate, as the temperature during laser irradiation is high, causing incipient melting of the sample. However, our study shows that products of ion irradiation are strongly affected by the temperature of the irradiated surface. The olivine used in this study contains low iron concentration (Table 2), but not <1 wt% as predicted for the surface of Mercury. Future ion irradiation studies on olivine with ~1 wt% Fe need to be carried out to further understand the lower limit for production of npFe^0. Since there is also a latitudinal variation of temperature on the surface of Mercury, our experiment done at 450 °C is relevant only for equatorial regions. Again, further experiments need to be carried out to look at the threshold temperature for formation of npFe^0 during ion irradiation. Any He and possibly H that are implanted into the surface materials of Mercury by solar wind should diffuse out of the grains and could be transferred to the

exosphere through a different desorption process. This can be another source of He seen in the exosphere of Mercury.

5. Conclusions

Olivine crystals with low iron (Fe = 3 wt%) content were irradiated with He^+ ions under ambient conditions and at 450 °C. The TEM study of the ion-damaged layer showed (a) the presence of a ∼140 nm partially amorphous layer with numerous bubbles within the sample irradiated under ambient conditions and the (b) presence of a 150–160 nm thick polycrystalline layer with no bubbles and 1–5 nm sized nanoparticles of iron within the sample irradiated at 450 °C. Ion irradiation of olivine grains with ∼3 wt% Fe present in the equatorial regions of Mercury should have nanoparticles of iron up to 5 nm in size around them, and their concentration and size can change with latitude and longitude, due to the variation of temperature. In addition, flash heating of the ion-irradiated olivine grains due to impacting dust particles can further increase the size of nanoparticles of Fe. Ostwald ripening of iron nanoparticles must also be active on the surface of Mercury, but to understand the process, experimental measurements of the diffusion coefficient of Fe within an amorphous silicate matrix are needed. All the above factors will finally lead to the variation in size and abundance of nanoparticles of iron with latitude and longitude. The solar-wind-implanted He within the surface materials of Mercury will diffuse out of the regolith grains in the equatorial regions owing to high temperatures during the daytime and can escape to the exosphere through desorption.

Acknowledgments

We thank Tobias Krekeler and Lida Wang for their technical help during the TEM sample preparation and analysis. We also thank Dr. Dorothée Kleinschrot and Dr. Volker von Seckendorff from the Institute for Geography, University of Würzburg, Germany, for providing the olivine crystal used in this study. Parts of this research were carried out at IBC at the Helmholtz-Zentrum Dresden-Rossendorf e. V., a member of the Helmholtz Association. The authors thank two anonymous reviewers and the editor for very helpful suggestions that significantly improved the manuscript. The PhD thesis of S.P.D. is supported by HBNI, Department of Atomic Energy, India. This work is supported by the Scheme for Promotion of Academic and Research Collaboration (SPARC) Phase-3 grant (SPARC/2024–2025/SADEF/P3824) and RACS-ISRO NIT Patna grants.

ORCID iDs

Surya Snata Rout https://orcid.org/0000-0003-0359-7693

References

Bauch, K. E., Hiesinger, H., Greenhagen, B. T., & Helbert, J. 2021, Icar, 354, 114083
Bott, N., Thompson, M. S., Loeffler, M. J., et al. 2024, PSJ, 5, 248
Bradley, J., & Ireland, T. 1996, in ASP Conf. Ser. 104, Physics, Chemistry, and Dynamics of Interplanetary Dust, ed. B. A. S. Gustafson & M. S. Hanner (San Francisco, CA: ASP), 275
Bradley, J., & Ishii, H. 2008, A&A, 486, 781
Bradley, J. P. 1994, Sci, 265, 925
Brunetto, R., & Strazzulla, G. 2005, Icar, 179, 265
Caminiti, E., Lantz, C., Besse, S., et al. 2024, Icar, 420, 116191
Carrez, P., Demyk, K., Cordier, P., et al. 2002, M&PS, 37, 1599
Cerofolini, G., Corni, F., Frabboni, S., et al. 2000, Mater. Sci. Eng. R Rep., 27, 1
Chapman, C. R. 2004, AREPS, 32, 539
Chaves, L., & Thompson, M. 2022, EP&S, 74, 124
Cintala, M. J. 1992, JGR, 97, 947
David, M., Beaufort, M., & Barbot, J. 2003, JAP, 93, 1438
Deutsch, A. N., Neumann, G. J., Kreslavsky, M. A., et al. 2024, PSJ, 5, 16
Dohmen, R., Becker, H.-W., Meißner, E., et al. 2002, EJMin, 14, 1155
Dukes, C. A., Baragiola, R. A., & McFadden, L. A. 1999, JGR, 104, 1865
Fichtner, P. F. P., Peeva, A., Behar, M., et al. 2000, NIMPB, 161, 1038
Hapke, B. 1965, NYASA, 123, 711
Hapke, B. 1966, Optical Properties of the Moon's Surface, in The Nature of the Lunar Surface, ed. W. Heiss, D. Menzel, & J. O'Keefe (Baltimore, MD: Johns Hopkins Univ. Press), 141
Hapke, B. 1968, Sci, 159, 76
Hapke, B. 1973, Moon, 7, 342
Hapke, B. 2001, JGR, 106, 10039
Hapke, B., Danielson, G., Klaasen, K., & Wilson, L. 1975, JGR, 80, 2431
Heck, P. R., Ushikubo, T., Schmitz, B., et al. 2010, GeCoA, 74, 497
Jäger, C., Sabri, T., Wendler, E., & Henning, T. 2016, ApJ, 831, 66
James, C., Letsinger, S., Basu, A., et al. 2002, LPSC, 33, 1827
James, C., Letsinger, S., Wentworth, S., et al. 2003, LPSC, 34, 1992
Kallio, E., & Janhunen, P. 2003, GeoRL, 30, 1877
Keller, L. P., & Clemett, S. J. 2001, LPSC, 32, 2097
Keller, L. P., & McKay, D. S. 1993, Sci, 261, 1305
Keller, L. P., & McKay, D. S. 1997, GeCoA, 61, 2331
KenKnight, C. E., Rosenberg, D. L., & Wehner, G. K. 1967, JGR, 72, 3105
Laczniak, D. L., Thompson, M. S., Christoffersen, R., et al. 2021, Icar, 364, 114479
Lantz, C., Brunetto, R., Barucci, M. A., et al. 2017, Icar, 285, 43
Loeffler, M. J., Dukes, C. A., & Baragiola, R. A. 2009, JGRE, 114, E03003
Loeffler, M. J., Dukes, C. A., Christoffersen, R., et al. 2016, M&PS, 51, 261
Lucey, P. G., & Noble, S. K. 2008, Icar, 197, 348
Lucey, P. G., & Riner, M. A. 2011, Icar, 212, 451
McCoy, T. J., Peplowski, P. N., McCubbin, F. M., & Weider, S. Z. 2018, in Mercury: The View after Messenger, ed. S. C. Solomon et al., 176 (Cambridge: Cambridge Univ. Press)
Moroz, L. V., Starukhina, L. V., Rout, S. S., et al. 2014, Icar, 235, 187
Morris, R. V. 1978, LPSC, 9, 2287
Nash, D. B. 1967, JGR, 72, 3089
Noble, S. K., Keller, L. P., & Pieters, C. M. 2005, M&PS, 40, 397
Noble, S. K., Keller, L. P., & Pieters, C. M. 2010, M&PS, 45, 2007
Noble, S. K., & Pieters, C. M. 2003, SoSyR, 37, 31
Noble, S. K., Pieters, C. M., & Keller, L. P. 2007, Icar, 192, 629
Noguchi, T., Kimura, M., Hashimoto, T., et al. 2014, M&PS, 49, 188
Noguchi, T., Nakamura, T., Kimura, M., et al. 2011, Sci, 333, 1121
Ono, K., Miyamoto, M., Kurata, H., et al. 2019, JAP, 126, 135106
Pieters, C. M. 1998, IGRv, 40, 981
Pieters, C. M., Fischer, E. M., Rode, O., & Basu, A. 1993, JGR, 98, 20817
Pieters, C. M., & Noble, S. K. 2016, JGRE, 121, 1865
Pieters, C. M., Taylor, L. A., Noble, S. K., et al. 2000, M&PS, 35, 1101
Raineri, V., Coffa, S., Szilagyi, E., et al. 2000, PhRvB, 61, 937
Rosenberg, D., & Wehner, G. 1964, JGR, 69, 3307
Sasaki, S., Hiroi, T., Nakamura, K., et al. 2002, AdSpR, 29, 783
Shimada, Y., Ikeda, Y., Yoshida, K., et al. 2022, JAP, 131, 165902
Sigmund, P. 1979, JAP, 50, 7261
Starukhina, L. V., & Shkuratov, Y. G. 2011, LPSC, 42, 1144
Stojic, A. N., Weber, I., Morlok, A., et al. 2023, Icar, 391, 115344
Thompson, M. S., Christoffersen, R., Zega, T. J., & Keller, L. P. 2014, EP&S, 66, 89
Thompson, M. S., Loeffler, M. J., Morris, R. V., et al. 2019, Icar, 319, 499
Thompson, M. S., Vander Kaaden, K. E., Loeffler, M. J., et al. 2021, LPSC, 52, 1496
Thompson, M. S., Zanetta, P-M., Zega, T. J., et al. 2022, LPSC, 53, 2134
Trang, D., Lucey, P. G., & Izenberg, N. R. 2017, Icar, 293, 206
Weber, I., Reitz, M. P., Morlok, A., et al. 2023, Icar, 404, 11563
Wehner, G., Kenknight, C., & Rosenberg, D. 1963, P&SS, 11, 1257
Wilson, J. T., Lawrence, D. J., Peplowski, P. N., & Feldman, W. C. 2019, JGRE, 124, 721
Wurz, P., Gamborino, D., Vorburger, A., & Raines, J. M. 2019, JGRA, 124, 2603
Yamada, M., Sasaki, S., Nagahara, H., et al. 1999, EP&S, 51, 1255
Yin, L., Ghose, S., & Adler, I. 1972, JGR, 77, 1360
Yin, L., Tsang, T., & Adler, I. 1975, LPSC, 6, 3277
Zaluzec, N. J. 1979, Quantitative X-Ray Microanalysis: Instrumental Considerations and Applications to Materials Science, in Introduction to Analytical Electron Microscopy, ed. J. J. Hren, J. I. Goldstein, & D. C. Joy (Boston, MA: Springer), 121